

## Research Article

# Study on Microscopic Roadbed Grouting Mechanism Based on CFD-DEM Coupling Algorithm

Changwei Yang <sup>1,2</sup>, Jinhao Guo,<sup>2</sup> Jing Lian <sup>3</sup> and Zhimeng Wang<sup>4</sup>

<sup>1</sup>Institute of Science and Technology, China Railway Eryuan Engineering Group Co., Ltd., Chengdu 610031, China

<sup>2</sup>Dept. of Civil Engineering, Southwest Jiaotong University, Chengdu 610031, China

<sup>3</sup>Dept. of Engineering Economics, Design Institute of China Railway Academy Co., Ltd., Chengdu 610031, China

<sup>4</sup>Dept. of Engineering, China Railway Eryuan Engineering Group Co., Ltd., Chengdu 610031, China

Correspondence should be addressed to Jing Lian; [lianjingswjtu@163.com](mailto:lianjingswjtu@163.com)

Received 15 February 2019; Revised 7 May 2019; Accepted 11 June 2019; Published 20 March 2020

Guest Editor: Qijun Zheng

Copyright © 2020 Changwei Yang et al. This is an open access article distributed under the Creative Commons Attribution License, which permits unrestricted use, distribution, and reproduction in any medium, provided the original work is properly cited.

Grouting reinforcement technology gradually has been widely used to repair the subgrade settlement diseases, but the current single application of discrete element software or finite element software cannot effectively simulate the grouting process. Therefore, one new method is put forward in the research of grouting based on the CFD-DEM coupling principle. And then, one typical subgrade section in the Shanghai–Nanjing intercity railway is used to simulate the grouting process and diffusion mechanism of slurry from microlevel. Based on the results of site survey, some findings are shown as follows: First, the new method is feasible which integrates the favorable aspects of discrete elements, finite elements, and boundary elements. Second, the greater the grouting pressure, the greater the influence range of grouting, and it shows six petals shape. When the grouting pressure is small, the grouting generally shows penetration or extrusion grouting, and its influence range is small. When the grouting pressure is large enough, it is characterized by splitting grouting, and the influence range of grouting is getting larger and larger. Third, the growth rates of influence range gradually increase with the increasement of grouting pressures, and the reasonable selection of grouting pressures is very important.

## 1. Introduction

With its outstanding characteristics of all-weather, high speed, high comfort performance, low energy consumption, and low pollution, the high-speed railway has become the preferred popular transportation mode for building a resource-saving, environment-friendly, and low-carbon society in China [1–4]. By the end of 2016, China's high-speed railway operation mileage has exceeded 22,000 km, and it is planned that by 2020, the high-speed railway will reach 30,000 km, covering over 80% of the major cities. And then, subgrade post-construction settlement deformation control is a prerequisite for ensuring safe, comfortable, and smooth operation of high-speed trains, but the settlement difference between the bridge and subgrade has exceeded 35 mm in some places [5, 6].

When the subgrade postconstruction settlement exceeds the limit, the grouting reinforcement technology has a kind of major solution and method, which have been widely used in the disease treatment of subgrade settlement [7–10]. However, because of the complexity and concealment of soil itself, the research progress of grouting reinforcement technology has stuck in the stage of theoretical lag behind practice, and the methods of site survey and laboratory experiments cannot reveal the diffusion mechanism of slurry. Numerical simulation analysis has become the most effective way to study grouting [11–18]. However, the grouting process is a two-way complicated action of soil and slurry. For the current application of discrete element software or finite element software, it cannot effectively simulate the obstruction of soil in the grouting process. This research team proposed to use CFD-DEM coupling to close the diffusion path of slurry in the whole process of grouting.

## 2. Site Survey

Taking some sections in Shanghai–Nanjing intercity railway as an example, the on-site monitoring work on the Shanghai–Nanjing intercity railway has been finished [19]. And then, the full line foundation settlement curve of the Shanghai–Nanjing intercity railway subgrade is obtained. In order to facilitate the analysis of the trend of the whole line foundation settlement, the accumulated settlement amount will be divided into 4 for bulging, 0 to 5, 5 to 10, 10 to 15 mm, and greater than 15 mm, and the sections are separately counted, as shown in Figure 1.

Figure 1 shows that the cumulative settlement of the whole line-based operation period is mostly less than 10 mm, and the cumulative settlements of the uplink line and downlink line are mainly concentrated at 0 to 5 mm (uplink line accounts for 66.92% and downlink line accounts for 47.8%), and the local hump of subgrade is obvious. The downlink line upheaval values concentrate at 2 mm to 3 mm, and only the upheaval values of a few of sections are greater than 5 mm. Based on the settlement results of full line, the overall settlement of Shanghai–Nanjing intercity railway is small and the line is stable. Only a very small number of sections have exceeded the settlement limit.

Based on that, in order to solve the shortcomings of the existing research and solve the problem of the current roadbed settlement, the maximum settlement point of the Shanghai–Nanjing intercity railway was selected. In this paper, Fluent-EDEM fluid-solid coupling method is proposed to simulate the grouting process. The grouting process and the effect of grouting on soil are analyzed from the microlevel, and the diffusion mechanism of grouting is revealed, which lays a foundation for guiding practical engineering.

## 3. Fundamental

**3.1. Discrete Element Contact Model.** Combined with the advantages of discrete elements and finite elements, a new method is put forward based on the CFD-DEM coupling principle, which can simulate the roadbed grouting treatment accurately [20, 21].

Firstly, select the soil contact model to study the damage of the meso-contact force of grouting. EDEM provides a variety of particle contact models for selection, such as Hertz–Mindlin contact model, Hertz–Mindlin bond model, and Hertz–Mindlin heat transfer model. In this paper, the Hertz–Mindlin bonding model (Hertz–Mindlin with bonding model) was used to simulate the soil.

The contact force and moment in the model can be decomposed into normal vectors ( $F^n$ ,  $M^n$ ) and tangential vector ( $F^s$ ,  $M^s$ ). In the parallel bond model, normal stiffness ( $N \cdot m^3$ ) and tangential stiffness ( $N \cdot m^3$ ) are  $k^n$ ,  $k^s$ , normal tensile strength ( $N \cdot m^{-2}$ ) and tangential shear strength ( $N \cdot m^{-2}$ ) are  $\bar{\sigma}_c$ ,  $\bar{\tau}_c$ , and the radius of the bonding area is  $R$ .

Within one-time step, the contact normal and tangential increments resulting from the contact displacement increment are

$$\begin{aligned}\Delta F^n &= -k^n A \Delta u^n, \\ \Delta F^s &= -k^s A \Delta u^s,\end{aligned}\quad (1)$$

where  $A = \pi R^2$  is the equivalent disc area,  $\Delta u^n$  is the normal direction of displacement, and  $\Delta u^s$  is the tangential increment.

The normal and tangential increments of the contact torque generated by the incremental rotation are

$$\begin{aligned}\Delta M^n &= -k^n J \Delta \theta^n, \\ \Delta M^s &= -k^s J \Delta \theta^s,\end{aligned}\quad (2)$$

where  $J = (1/2)\pi R^4$  is the moment of inertia passing through the contact point for the equivalent disc cross-section with the  $\Delta \theta^s$  direction as the axis and  $\Delta \theta^n$  and  $\Delta \theta^s$  are the direction of rotation increment and tangential increment.

According to the beam theory of material mechanics, the formula for calculating the maximum tensile stress and shear stress acting on the equivalent disk is

$$\sigma_{\max} = \frac{|F^n|}{A} + \frac{|M^s|}{I} R, \quad (3)$$

$$\tau_{\max} = \frac{|F^s|}{A} + \frac{|M^n|}{I} R. \quad (4)$$

In formulas (3) and (4),  $R$  is the contact radius of the particle, which is set to 3.5 mm in this study.

In EDEM, the particle cohesion between particles is determined by critical normal stress, the tangential bond strength, and bonded disk radius between particles. If  $\bar{\sigma}_{\max} \geq \bar{\sigma}$  or  $\bar{\tau}_{\max} \geq \bar{\tau}$ , the contact keys will be damaged.

**3.2. Fluid-Particle Interaction Force.** In CFD-DEM coupling algorithm, there are some mechanical models used to calculate the particle-fluid interaction force, such as drag model, lift model, and interfacial heat transfer models [22, 23]. At the same time, this study focuses on the soil particle-slurry interaction forces which are mainly drag forces. Therefore, the Di-Felice drag model [24] is selected and used to calculate the particle-fluid interaction force, and it can consider the interaction among particles by introducing volume fractions of a single particle, which is used in other similar studies [25, 26]. The Di-Felice drag model is shown as follows:

$$\begin{aligned}F_d &= \frac{\pi(d_p)^2}{2} C_D \rho_f |v_f - v_s| (v_f - v_s) \varepsilon_s^{-(\chi+1)}, \\ \chi &= 3.7 - 0.65 \exp\left[-\frac{(1.5 - \log 10 \text{Re}_s)^2}{2}\right], \\ C_D &= (0.63 + 4.8\sqrt{\text{Re}_s})^2.\end{aligned}\quad (5)$$

In the above formulas,  $d_p$  is the particle diameter,  $C_D$  is the drag coefficient of a single particle,  $\rho_f$  is the fluid phase density,  $\varepsilon_s$  is the volume fraction of the particle phase,  $v_f$  is

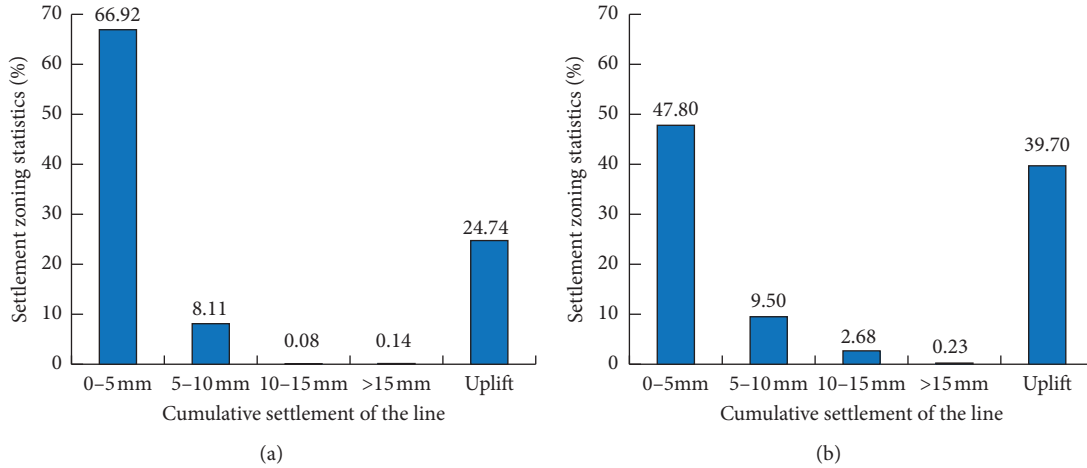


FIGURE 1: Settlement zoning statistics. (a) Uplink line (b) Downlink line.

the fluid phase velocity at the particle center,  $v_s$  is the particle phase velocity, and  $Re_s$  is the particle Reynolds number.

#### 4. Calculation Model and Parameters

**4.1. Calculation Model.** Based on the results of site survey, some soil samples in the research region are selected to finish the granule screening tests, and the results are shown in Figure 2. Strictly speaking, the maximum diameter  $R_{\max}$  is 10 mm–20 mm and the minimum diameter  $R_{\min}$  is 0.075 mm. And then, 10 mm is selected as the  $R_{\max}$  in order to study the diffusion mechanism in more detail. The approximate average diameter  $R_{\text{average}}$  of all particles is  $(R_{\max} + R_{\min})/2 = (10 \text{ mm} + 0.075 \text{ mm}) = 5.0375 \text{ mm}$  after some tests. And then, particle diameter 6 mm is selected as the  $R_{\text{average}}$  based on the consideration of calculation amount and calculation precision. In order to simulate the heterogeneous distribution of soil particles in the model precisely, the particle diameters are randomly generated from  $R_{\min}$  to  $R_{\max}$  based on their different mass proportion in the model. The number of particles is controlled by void ratio  $e$  which should be set in the calculation program, and it can be calculated approximately by using the following method. The aforementioned research thought has been used in other similar studies [27–31]:

$$e = \frac{2bh\bar{r} - \sum_{i=1}^N (4/3)\pi r_i^3}{\sum_{i=1}^N (4/3)\pi r_i^3}. \quad (6)$$

In the above formulas,  $e$  is the void ratio,  $b$  is the width of model,  $h$  is the height of the model,  $N$  is the total number of particles, and  $r_i$  is the radius of every particle.

As shown in Figure 3, the model has a length of 60 cm, a width of 60 cm, and a height of 30 cm, and the radius of the grouting pipe is 4 cm. In order to simulate the real grouting, six grouting holes are opened at 4 cm from the bottom of the grouting pipe, and the radius of the holes is 1 cm, and a total of 599044 particles are filled. The model is surrounded by a wall, and the particles are not allowed to escape from the inside of the model. The mechanical parameters of the particles and the wall are selected as default values.

**4.2. Setup Parameters.** In the actual project, there is soil confining pressure around the grouting holes. Since the simulation does not consider the influence of the confining pressure of the soil, the mesoscopic parameters of the soil are corrected [32–34], and the soil calculation parameters are shown in Table 1.

The grouting material adopts cement slurry with a water-cement ratio of 0.8 : 1, and its parameter setting in Fluent is shown in Table 2.

In this simulation, because the engineering design grouting speed is 20 L–30 L/min, the simplified model cannot be calculated because of too many discrete element particles. Because of the gap between the actual project and the simulation, in this model, the grouting condition based on the grouting amount can be used to calculate the grouting time of the simulation. It is more suitable to calculate the grouting time to be 0.5 s. In this paper, according to the actual engineering requirements, the damage of contact bonds under 7 different grouting pressures was simulated, which were 0.1 MPa, 0.15 MPa, 0.2 MPa, 0.25 MPa, 0.3 MPa, 0.4 MPa, and 0.5 MPa, respectively.

#### 5. Analysis of Calculation Results

**5.1. Flow Field under Different Grouting Pressures.** With the increase of grouting pressures, the diffusion range of slurry and its growth rates gradually increases, as shown in Figure 4. The reason of the aforementioned phenomenon may be related to the destruction of soil, which has been shown in Figure 5.

Figure 5 shows that the soil particle inhibits the diffusion of slurry obviously. The greater the grouting pressure, the greater the influence range of grouting which shows six petals shape. When the grouting pressure is small, there is only a little damaged contact bond around the grouting holes, and the grouting generally shows penetration or extrusion grouting whose influence range is small. When the grouting pressure is large enough, the damaged contact bond gradually increases and it is characterized by splitting grouting. At the same time, the influence range of grouting is

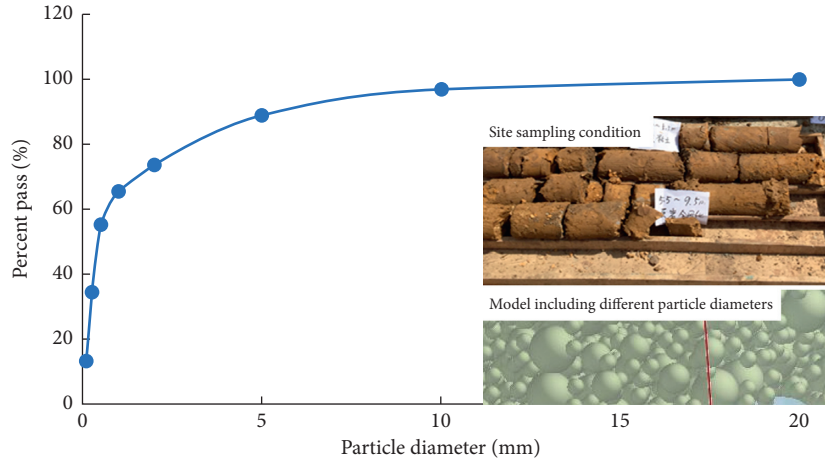


FIGURE 2: Granule screening test results and some other related information.

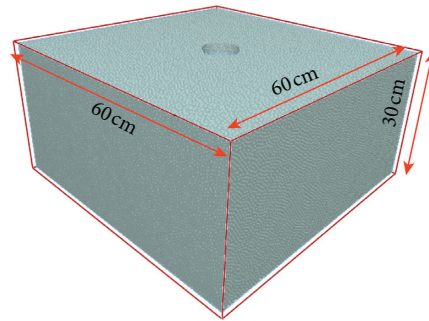


FIGURE 3: Model after particle filling.

TABLE 1: Particle simulation parameters.

Particle diameter (mm)	6
Static friction coefficient	0.4
Density ( $\text{kg}/\text{m}^3$ )	1920
Poisson's ratio	0.28
Gravity acceleration ( $\text{m}/\text{s}^2$ )	9.81
Parallel bond stiffness ( $\text{N}/\text{m}^3$ )	$1.50E+06$
Normal bond stiffness ( $\text{N}/\text{m}^3$ )	$1.50E+06$
Normal critical stress (Pa)	$2.00E+08$
Tangential critical stress (Pa)	$2.00E+08$

TABLE 2: Slurry parameter in Fluent.

Density ( $\text{kg}/\text{m}^3$ )	Cement viscosity	Specific heat capacity ( $\text{J}/\text{kg}\cdot\text{K}$ )
1760	0.06	840

getting larger and larger, and every grouting hole gradually shows an alluvial fan.

**5.2. Grouting Influence Range under Different Grouting Pressures.** The grouting process is a two-way process between the slurry and the soil. When the grouting pressure is small, the performance is osmotic grouting. When the pressure of the grouting is gradually increased, it is expressed as extrusion or even splitting.

Based on the actual engineering, this paper selects seven working conditions for simulation to compare the influence range of grouting under different pressures. As shown in Figure 6, the damage range of the contact keys under the respective grouting pressures is given.

It can be seen from Figure 6 that when the grouting pressure is 0.1 MPa, the concentrated rupture radius of the contact bond is only 1.6 cm. As the grouting pressure increases, the rupture bond grouting is also gradually increased. When the pressure is increased to 0.5 MPa, the radius of influence of the contact key is increased to 25 cm.

**5.3. Damage of Contact Keys under Different Grouting Pressures.** In the calculation process, in order to understand the damage of the contact keys in different ranges of the model, a geometry section is set within a certain range, a monitoring circle is set every at 5 cm, and a total of five monitoring circles are set for easy identification of each monitoring circle, respectively, from the inside to the outside, numbered 1, 2, 3, 4, and 5, as shown in Figure 7.

Table 3 shows the damage of the contact keys at the end of the simulation for each large monitoring circle, and Figure 8 shows the percentage of contact bond damage in monitoring circles 1–5. It can be seen that the greater the grouting pressure, the greater the number of damages in

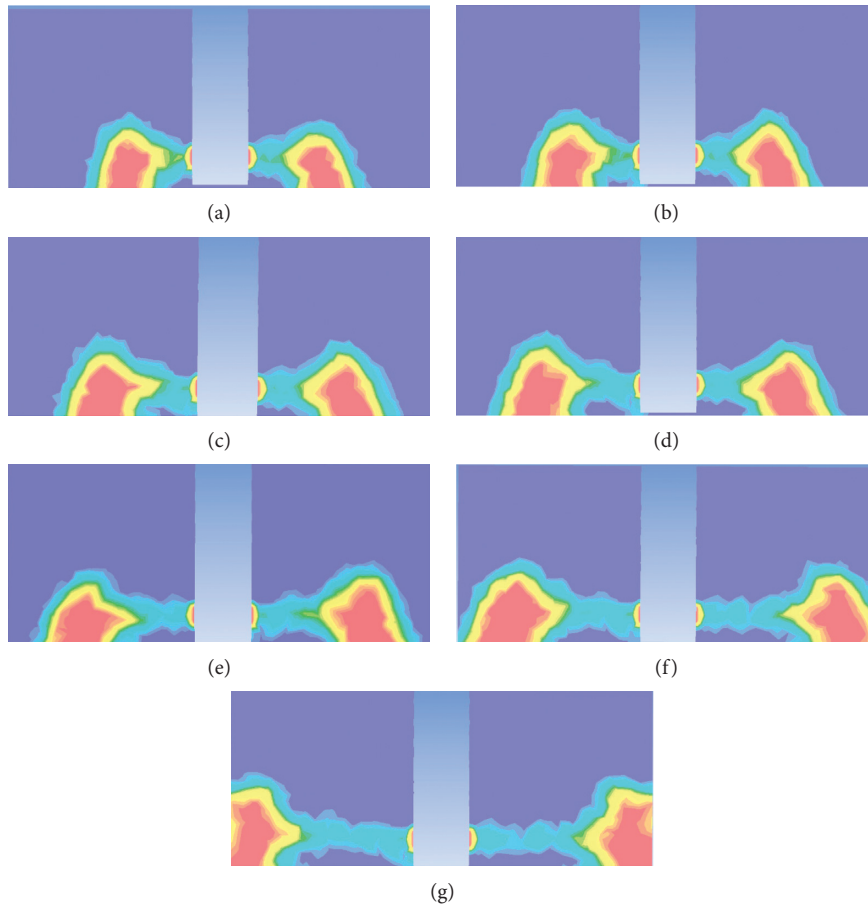
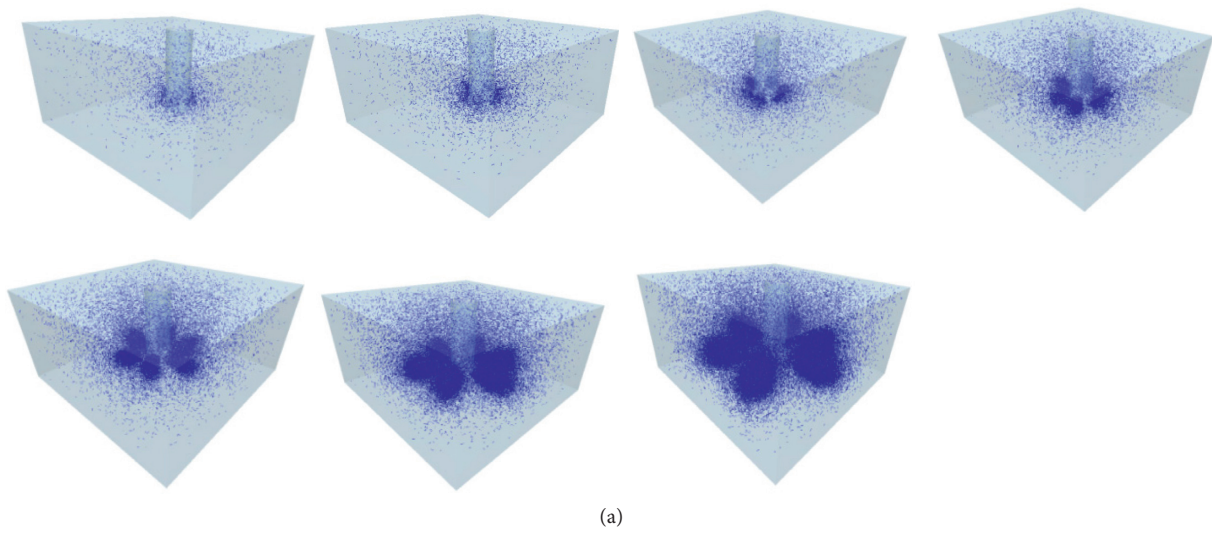


FIGURE 4: Diffusion range of slurry under different pressures (0.1 MPa, 0.15 MPa, 0.2 MPa, 0.25 MPa, 0.3 MPa, 0.4 MPa, and 0.5 MPa).



(a)  
FIGURE 5: Continued.

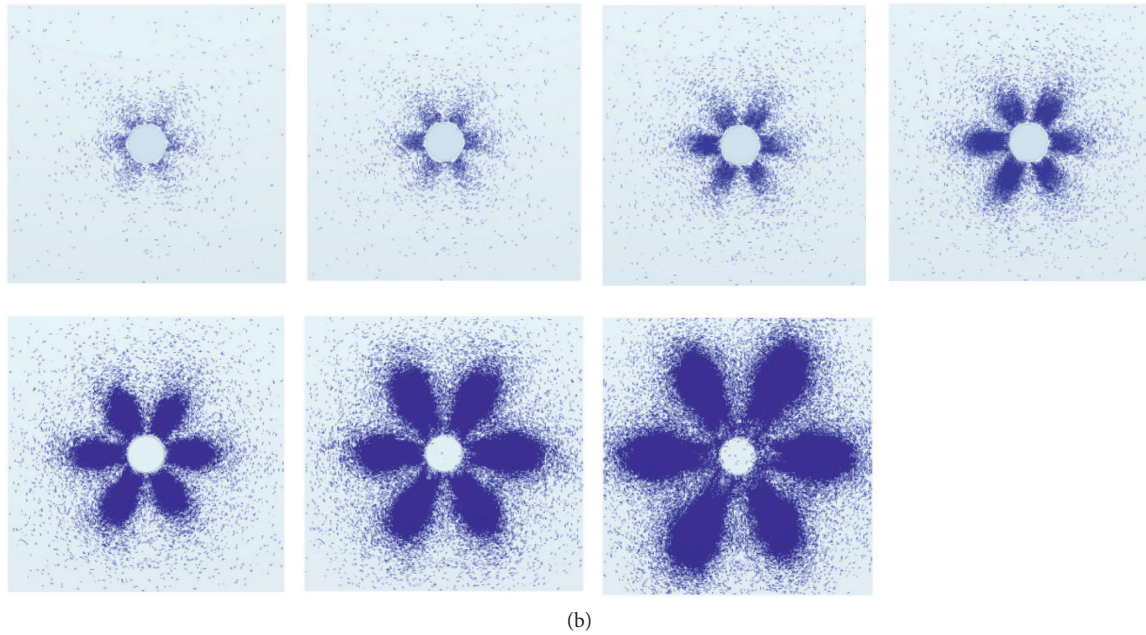


FIGURE 5: Damage range of contact keys under different grouting pressures. (a) The damage of the overall contact bond under different pressures (0.1 MPa, 0.15 MPa, 0.2 MPa, 0.25 MPa, 0.3 MPa, 0.4 MPa, and 0.5 MPa). (b) Destruction of plane contact keys of grouting holes under different pressures (0.1 MPa, 0.15 MPa, 0.2 MPa, 0.25 MPa, 0.3 MPa, 0.4 MPa, and 0.5 MPa).

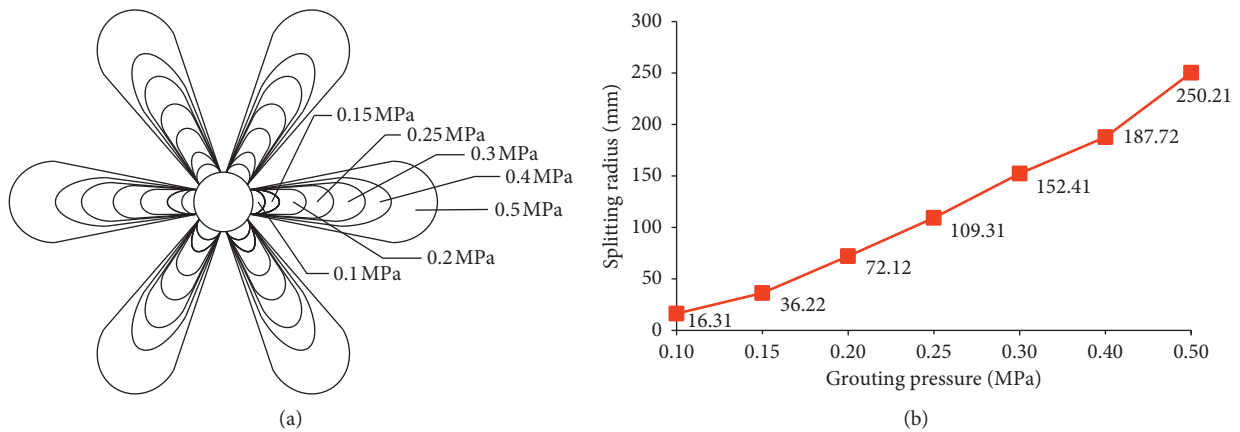


FIGURE 6: Variation of the splitting radius with grouting pressure. (a) Variation of splitting radius under different grouting pressures. (b) Variation of grouting radius with grouting pressure.

each monitoring circle. When the grouting pressure exceeds 0.4 MPa, the number of contact bond damage in the No. 1 monitoring circle is actually less. As shown in Figure 8, the maximum number of contact keys that rupture at 0.1 MPa is 2.99% of the monitoring circle at the No. 1 monitoring circle. The number of contact keys broken at 0.15 MPa accounted for the largest monitoring circle in the monitoring circle, which accounted for 5.45%. The number of contact keys that rupture at 0.2 MPa accounts for the largest in the monitoring circle, which is 7.33% of the monitoring circle No. 1. The number of contact keys that rupture at 0.25 MPa accounts for the largest monitoring circle in the No. 1 monitoring circle, accounting for 19.63%. The maximum number of contact

bonds that rupture at 0.3 MPa is 37.05% of the No. 2 monitoring circle. The number of contact keys that rupture at 0.4 MPa accounts for the largest monitoring circle in the No. 3 monitoring circle, and the value is 58.59%. When the grouting pressure is 0.5 MPa, the number of broken contact keys occupies the largest monitoring circle in the monitoring circle, and the ratio of the total contact keys is 84.30%.

Simulated grouting shows that when the grouting pressure is very small, the grouting performance is penetration or extrusion grouting, and the damage of the slurry to the soil is also small. When the grouting pressure gets larger and larger, the damage effect of the slurry on the soil bond is more and more obvious, which is characterized by splitting.

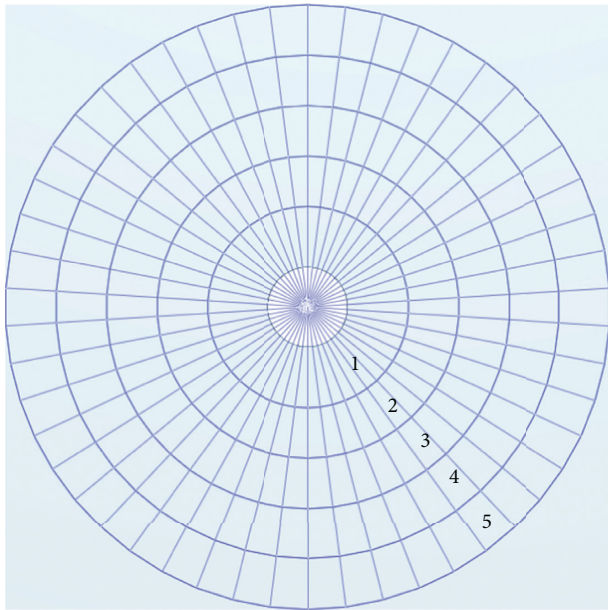


FIGURE 7: Number of monitoring circle.

TABLE 3: Number of contact key failures in each monitoring circle.

Grouting pressure	Number of monitoring circles				
	1	2	3	4	5
0.1 MPa	1571	2024	2205	2308	2381
0.15 MPa	2858	3682	3985	4155	4270
0.2 MPa	5863	7522	8098	8399	8575
0.25 MPa	10301	15425	16693	17224	17471
0.3 MPa	12458	29623	33449	34718	35242
0.4 MPa	8496	42214	65550	70423	72009
0.5 MPa	7845	31611	87043	120956	128564

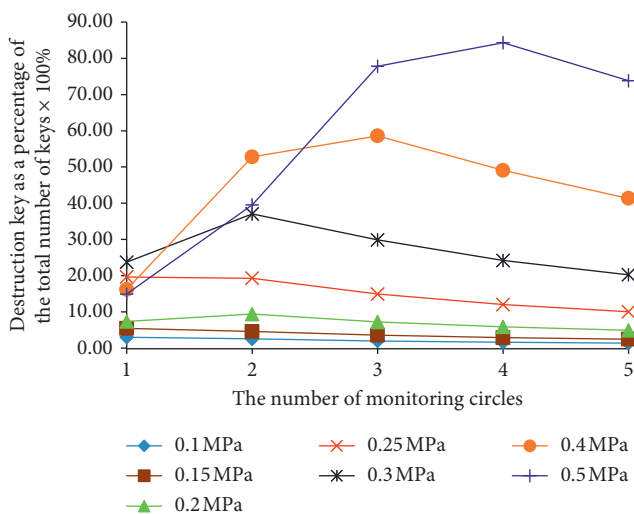


FIGURE 8: Proportion of broken bonds under different grouting pressures.

### 6. Conclusion

In this paper, the Fluent-EDEM coupling method is used to simulate the grouting process. The EDEM discrete element software is used to simulate the soil. The Fluent fluid software is used to simulate the slurry. Through the simulations, there are some conclusions as shown in the following:

- (1) Combined with the advantages of discrete elements and finite elements, a new method is put forward based on the CFD-DEM coupling principle, which can simulate the roadbed grouting treatment accurately.
- (2) The soil particle inhibits the diffusion of slurry obviously. The greater the grouting pressure, the greater the influence range of grouting, and it shows six petals shape. When the grouting pressure is small, the grouting generally shows penetration or extrusion grouting, and its influence range is small. When the grouting pressure is large enough, it is characterized by splitting grouting, and the influence range of grouting gets larger and larger.
- (3) The growth rates of influence range gradually increase with the increasement of grouting pressures, and its reason may be related to the destruction of soil, which will seriously affect the impact of grouting reinforcement. Therefore, reasonable selection of grouting pressures is very important.

The fluid-solid coupling idea of CFD-DEM is used to simulate the grouting process by using Fluent-EDEM coupling, which provides new ideas and new methods for grouting research. However, due to the fact that software technology is still not mature enough, this method still has certain disadvantages in simulating grouting. For example, the number of particles calculated by the discrete element itself is limited. But it is still a good new way to study grouting.

### Data Availability

The data used to support the findings of this study are available from the corresponding author upon request.

### Conflicts of Interest

The authors of this study do not have any conflicts of interest regarding the publication of this article.

### Acknowledgments

This study was supported in part by China Railway Eryuan Engineering Group Co., Ltd. Scientific Research Project (no. KYY2017069(17-17)); Sichuan Provincial Science and Technology Support Project (no. 2019JDRC0133, 2018JY0549, 18MZGC0247, and 18MZGC0186); Science and Technology Research and Development Plan of China National Railway Corporation Limited (N2019G022); and 2018 Sichuan Provincial Ten Thousand Program Project.

## References

- [1] R. Chen, X. Zhao, Z. Wang, H. Jiang, and X. Bian, "Experimental study on dynamic load magnification factor for ballastless track-subgrade of high-speed railway," *Journal of Rock Mechanics and Geotechnical Engineering*, vol. 5, no. 4, pp. 306–311, 2013.
- [2] X. Chapeleau, T. Sedran, L.-M. Cottineau et al., "Study of ballastless track structure monitoring by distributed optical fiber sensors on a real-scale mockup in laboratory," *Engineering Structures*, vol. 56, no. 11, pp. 1751–1757, 2013.
- [3] Y. Shan, B. Albers, and S. A. Savidis, "Influence of different transition zones on the dynamic response of track-subgrade systems," *Computers and Geotechnics*, vol. 48, pp. 21–28, 2013.
- [4] C. Yang, J. Zhang, Z. Wang, J. Hou, and C. Si, "Model test of failure modes of high embankment and aseismic measures for buried strike slip fault movement," *Environmental Earth Sciences*, vol. 77, no. 6, pp. 1–8, 2018.
- [5] C. Yang, X. Tong, J. Zhang, and H. Zhu, "A new design of bridge-subgrade transition sections applied in Beijing-Shanghai high-speed railway," *Complexity*, vol. 2018, Article ID 1249092, 11 pages, 2018.
- [6] Y. Guo and W. Zhai, "Long-term prediction of track geometry degradation in high-speed vehicle-ballastless track system due to differential subgrade settlement," *Soil Dynamics and Earthquake Engineering*, vol. 113, no. 10, pp. 1–11, 2018.
- [7] Z. Shen and L. Xu, "Research of stability effect on adjacent existing railing lines due to new line construction," *Journal Of Railway Science And Engineering*, vol. 11, no. 1, pp. 93–100, 2014.
- [8] Z. Shen and L. Xu, "Dynamic analysis on influence of high-speed railway construction on existing adjacent railway lines and countermeasures," *Journal of The China Railway Society*, vol. 35, no. 6, pp. 82–90, 2013.
- [9] Y. Tian, J. Liu, Y. Wu, X. Guifu, and X. Jin, "Numerical simulation analysis of grouting in water-rich sand stratum by three-dimensional particle flow software," *Municipal Technology*, vol. 33, no. 6, pp. 68–71, 2015.
- [10] M. Zhou, *Experimental Study on Diffusion Law with Horizontal Hole Grouting Reinforcement in Shallow Sand Layer*, China Coal Research Institute, Beijing, China, 2018.
- [11] G. Gustafson, J. Claesson, and Å. Fransson, "Steering parameters for rock grouting," *Journal of Applied Mathematics*, vol. 2013, no. 1, Article ID 269594, 9 pages, 2013.
- [12] H. Stille, G. Gustafson, and L. Hassler, "Application of new theories and technology for grouting of dams and foundations on rock," *Geotechnical and Geological Engineering*, vol. 30, no. 3, pp. 603–624, 2012.
- [13] Q. Gu, S. Zhang, X. An, and Y. Zhang, "Research on characteristics of rock debris explosion based on coupled FLUENT-EDEM," *Explosion and Shock*, vol. 36, no. 5, pp. 611–616, 2016.
- [14] H. Li, Y. Li, Z. Tang, L. Xu, and Z. Zhao, "Numerical simulation and analysis of vibration screening based on EDEM," *Journal of Agricultural Engineering*, vol. 27, no. 5, pp. 117–121, 2011.
- [15] S. Li, W. Zhan, Q. Zhang et al., "Research on advantage-fracture grouting mechanism and controlled grouting method in water-rich fault zone," *Geotechnical*, vol. 35, no. 3, pp. 744–752, 2014.
- [16] L. Zhou, W. Luo, H. Wu, and H. Liu, "Coupled simulation of sulfur deposition in sour gas reservoir formation based on EDEM-FLUENT," *Fault Block Oil and Gas Field*, vol. 23, no. 2, pp. 213–215, 2016.
- [17] P. Qin, "Micromechanics particle flow numerical simulation on sandy soil grouting," *Journal of Civil Engineering and Management*, vol. 34, no. 4, pp. 30–38, 2017.
- [18] H. Wu, J. Xia, G. Zhang, P. Wang, S. Lao, and X. Zhang, "Design and experiment of spin-jet flow type lotus root digging machine based on EDEM-fluent," *Journal of Agricultural Engineering*, vol. 4, no. 5, pp. 9–14, 2018.
- [19] M. Zhou, Y. Shang, L. Xu, and H. Chen, "Control measures for settlement overrun of high-speed railway subgrade during operation period and effect evaluation," *Railway Standard Design*, vol. 61, no. 12, pp. 28–34, 2017.
- [20] X. Du, Q. Zhang, Y. Kong, and C. Chen, "Frost heave mechanism analysis of coarse grained soil for high speed railway subgrade," *Chinese Journal of Underground Space and Engineering*, vol. 12, no. S1, pp. 152–156, 2016.
- [21] B. Indraratna, S. Nimbalkar, and H. Rujikiatkamjorn, "From theory to practice in track geomechanics—Australian perspective for synthetic inclusions," *Transportation Geotechnics*, vol. 1, no. 4, pp. 171–187, 2018.
- [22] N. G. Deen, M. V. S. Annaland, M. A. V. D. Hoef, and J. A. M. Kuipers, "Review of discrete particle modeling of fluidized beds," *Chemical Engineering Science*, vol. 62, no. 1–2, pp. 28–44, 2007.
- [23] Z. Zhang, T. Yin, X. Huang, and D. Dias, "Slurry filtration process and filter cake formation during shield tunnelling: insight from coupled CFD-DEM simulations of slurry filtration column test," *Tunnelling And Underground Space Technology*, vol. 87, no. 5, pp. 64–77, 2019.
- [24] R. D. Felice, "The voidage function for fluid-particle interaction systems," *International Journal of Multiphase Flow*, vol. 20, no. 1, pp. 153–159, 1994.
- [25] P. D. Bonkinpillewar, A. Kulkarni, M. V. Panchagnula, and S. Vedantam, "A novel coupled fluid-particle DEM for simulating dense granular slurry dynamics," *Granular Matter*, vol. 17, no. 4, pp. 511–521, 2015.
- [26] Z. Wang, Y. Teng, and M. Liu, "A semi-resolved CFD-DEM approach for particulate flows with kernel based approximation and Hilbert curve based searching strategy," *Journal of Computational Physics*, vol. 384, no. 5, pp. 151–169, 2019.
- [27] S. WU, *Studies and application of ground treatment by composite anchor pile with pressure grouting*, Beijing University of Science and Technology, Beijing, China, 2004.
- [28] P. Tahmasebi and S. Kamrava, "A pore-scale mathematical modeling of fluid-particle interactions: thermo-hydro-mechanical coupling," *International Journal of Greenhouse Gas Control*, vol. 83, no. 4, pp. 245–255, 2018.
- [29] M. Jiang, Z. Shen, and D. Wu, "CFD-DEM simulation of submarine landslide triggered by seismic loading in methane hydrate rich zone," *Landslides*, vol. 15, no. 11, pp. 2227–2241, 2018.
- [30] Y. He, A. E. Bayly, A. Hassanpour, and H. Ali, "Coupling CFD-DEM with dynamic meshing: a new approach for fluid-structure interaction in particle-fluid flows," *Powder Technology*, vol. 325, no. 2, pp. 620–631, 2018.
- [31] K. W. Chu, J. Chen, B. Wang et al., "Understand solids loading effects in a dense medium cyclone: effect of particle size by a CFD-DEM method," *Powder Technology*, vol. 320, no. 10, pp. 594–609, 2017.
- [32] N. Yin, S. Li, Y. Shi, Z. Sun, and Z. Yin, "Discrete element analysis of the behavior of frozen loess cement under different confining pressures," *Glacier*, vol. 39, no. 4, pp. 858–867, 2017.
- [33] J. Liu, R. Liu, X. Zhang, and S. Li, "Diffusion law model test and numerical simulation of cement fracture grouting," *Journal of Rock Mechanics and Engineering*, vol. 31, no. 12, pp. 2445–2452, 2012.

- [34] J. C. O. Nielsen and X. Li, "Railway track geometry degradation due to differential settlement of ballast/subgrade—numerical prediction by an iterative procedure," *Journal of Sound and Vibration*, vol. 412, no. 1, pp. 441–456, 2018.